A solar cycle clock for extreme space weather

Sandra Chapman (S.C.Chapman@warwick.ac.uk)
University of Warwick https://orcid.org/0000-0003-0053-1584
Thierry Dudok de Wit
International Space Science Institute

Article

Keywords: solar cycle, space weather

Posted Date: January 5th, 2024

DOI: https://doi.org/10.21203/rs.3.rs-3672243/v1

Additional Declarations: There is **NO** Competing Interest.

A solar cycle clock for extreme space weather

Sandra Chapman[1,2,3*] and Thierry Dudok de Wit[2,4]

[1*]Centre for Fusion, Space and Astrophysics, Physics Department, University of Warwick, UK.
[2]International Space Science Institute, Bern, Switzerland.
[3]Department of Physics and Statistics, University of Tromso, Norway.
[4]LPC2E, University of Orléans/CNRS/CNES, France.

*Corresponding author(s). E-mail(s): S.C.Chapman@warwick.ac.uk;
Contributing authors: ddwit@issibern.ch;

Abstract

The variable solar cycle of activity is a long-standing problem in physics. It modulates the overall level of space weather activity at earth, which in turn can have significant societal impact. The Hilbert transform of the sunspot number is used to map the variable length, approximately 11 year Schwabe cycle onto a uniform clock. The clock is used to correlate extreme space weather seen in the ***aa*** index, the longest continuous geomagnetic record at earth, with the record of solar active region areas and latitudes since 1874. This shows that a clear switch-off of the most extreme space weather events occurs when the solar active regions move to within 15 degrees of the solar equator, from regions of high gradient in solar differential rotation which can power coronal mass ejections, to a region where solar differential rotation is almost constant with latitude. This overlaps with the onset of more moderate space weather events which coincide with 27 day solar rotation recurrences in the ***aa*** index, consistent with stable, persistent source regions. This offers a physical explanation for the longstanding identification of a two component cycle of activity in the ***aa*** index.

Keywords: solar cycle, space weather

1 Main

Extreme space weather storms have the potential for significant societal impact and financial loss (1; 2), disrupting power distribution, communication, aviation and satellites. Statistical estimates of the likelihood of occurrence of extreme space storms is central to decision making for mitigating the effects of space weather which necessarily must balance resilience against cost. Whilst the severity of the technological and societal impact of a geomagnetic storm depends on many factors (3), from the details of the structure emitted from the corona, its solar wind propagation, to how it interacts with earth's magnetosphere (4; 5; 6), the most extreme events are directly driven by, and directly correlate with, large-scale solar eruptions (7; 8; 9). Quantifying extreme space weather risk is thus intimately related to understanding the solar cycle of activity, which in turn is a longstanding unsolved problem in physics (4), informing our understanding of the solar dynamo which is as yet not complete (10).

Long-term observations over multiple solar cycles are essential to track solar cycle variability since no two cycles are of the same amplitude and duration. Figure 1 plots an overview of the long-term solar and geophysical records (see Methods) that are analysed in this Letter. The approximately 11 year Schwabe cycle is tracked by sunspot number observations for which monthly records are available from 1749. Panel (a) of Figure 1 plots the 13 month smoothed sunspot number (SSN) for the last 13 Schwabe cycles. Sunspot latitudes or more specifically, the latitudes of solar coronal active regions (ARs) (4) execute a classic butterfly pattern as shown in Figure 1 (b), emerging at mid-latitudes early in the Schwabe cycle and migrating towards the solar equator where their magnetic flux annihilates, as part of the birth of the next cycle. The time interval of our analysis, shown in Figure 1, begins at the start of the AR record.

Long-term ground based magnetometer observations at earth track the geomagnetic response to the solar cycle of activity (4; 7). The longest continuous record of the magnetic field at earth is provided by the *aa* index (11) which is plotted in panel (d) of Figure 1. Overall geomagnetic activity as seen in the *aa* index tracks the solar cycle variation in solar activity (12; 13), and overall levels of geomagnetic activity can be good solar cycle predictors (14; 15). The *aa* index is however highly discretized (16; 17); high fidelity geomagnetic data, available over the last 4-5 cycles confirm that the high quantiles of geomagnetic activity track the variation in solar activity both within and between solar cycles (17; 18; 19).

Although the details are complex, the overall picture of extreme geomagnetic storms is primarily driven by coronal mass ejections (CMEs) during solar cycle maximum, when the ARs are at higher solar latitudes, and by solar co-rotating high speed streams during the declining phase, when the ARs are at lower latitudes (7). This is reflected in the solar wind state which is more disordered at maximum (21). The declining phase is characterised by high speed streams in the solar wind (22) and recurrences in long-term geomagnetic indices on the 27 day solar rotation timescale (23; 24; 25; 26), as can be seen in the autocovariance of the *aa* index at 27 day lag plotted in Panel (e) of Figure 1. There are subtleties in identifying the coronal sources of CMEs and recurrent high speed streams; ARs and coronal holes are discriminated by coronal magnetograms, available over the last few cycles only (27). High speed streams may originate from corotating solar equatorial structures or polar coronal holes (22). Nevertheless, a reasonable working hypothesis for performing statistical correlations over multiple solar cycles is that the latitudes of the ARs provide an overall indicator of a range of latitudes from which CMEs and (non-polar) high speed streams originate.

CME initiation and evolution is complex (28; 29) however the overall source of energy of a 'normal' or 'standard' CME is understood to be the magnetic energy from strongly sheared magnetic field (30). The magnetic field is sheared by the differential rotation of the outer convective region of the sun. The axisymmetric differential rotation increases with decreasing latitude, maximising at the solar equator. The differential rotation varies only weakly across these low latitudes, varying in total by about 13% (see Methods) across latitudes $\pm 15^\circ$ of the equator (20; 31; 32). Since the meridional flow is 1-2 orders of magnitude weaker (32), this supports the overall picture that extreme eruptions initiated at mid latitudes are ultimately

powered by shearing of magnetic field driven by the latitudinal gradient in differential rotation, corresponding to more frequent and higher energy CMEs, so that CME rates roughly track the SSN (29) and are less energetic around solar minimum (33). Conditions around solar maximum then result in the most intense, CME driven geomagnetic activity. CME driven activity will decline as the ARs move to lower latitudes and geomagnetic activity will be more predominately driven by recurrent high speed streams which originate in regions of relatively low latitudinal gradient in differential rotation, either at the poles or at low latitudes, are not predominantly shear-driven, and are thus stable over multiple solar rotations. To see this overall effect in the AR record, panel (c) of Figure 1 colour codes each latitudinal bin containing a moderate-to large AR area ($> 50 \mu Hem$) with the level of activity in the *aa* geomagnetic index during each Carrington rotation (the panel is reproduced for other AR area thresholds in Figure ED2 which shows the same result). The colours indicate if within each Carrington rotation *aa* exceeds the levels [100,200,300,400,500,600] nT. The horizontal blue lines are at $\pm 15^\circ$ and whilst the colour coding indicates *all* latitudes at which there are ARs, the plots shows that the most intense events ($aa > 300nT$, orange, red, purple, black) only occur when there are a subset of ARs at latitudes above about 15° in either hemisphere, whereas when the ARs are all within 15° of the equator, the events are less intense ($aa < 300nT$, blue, green).

AR latitudes then in principle contain information on the likelihood of extreme space weather events over the solar cycle. Exploiting this requires systematic timing of the phase of the solar cycle, which is challenging given that no two cycles are of the same length. Normalizations of the SSN cycle onto a uniform timebase have included collapse of the SSN profile (4; 34) and the average modulus sunspot latitude (34). The Hilbert transform of the SSN record can be used to map the non- uniform duration solar cycle onto a uniform interval 2π of analytic phase (13), see Methods and Figure ED1. This provides a regular clock for the solar cycle which can be used to organise long-term observations of solar and geomagnetic activity. The Hilbert transform analytic phase acts as a single unifying parametric coordinate for different indicators of the state of solar activity across the solar cycle, and corresponding geomagnetic response at earth.

From the solar clock, a clear quiet interval in the solar cycle can be identified (13) which spans a uniform interval of $\sim 4\pi/5$ in analytic phase, centred on solar minimum. This quiet interval has a duration of of 4.4 years in an exactly 11 year cycle but is non uniform in time in the SSN record; these quiet intervals are indicated with grey shading on Figure 1. The switch-off and on of activity are identified at phase $\pm 2\pi/5$ in advance of, and following, the average phase of the cycle minima which have been identified in the SSN record of the last 25 solar cycles. The switch-on of activity at the end of the quiet interval approximately coincides with the average analytic phase over which the last 12 solar cycle terminators have occurred, these terminator times (35; 36; 37), are identified individually from multiple observations of coronal magnetic activity. The cycle termination is observed as an abrupt reduction in the density of EUV bright point density around the solar equator, marking the final cancellation of the old cycle (magnetic) activity bands at the equator (35), coinciding with the emergence of mid-latitude sunspots of the new solar cycle butterfly pattern.

The switch-off and switch-on of activity which bracket the quiet interval are however obtained solely from the SSN timeseries. Whilst they were originally identified from the SSN Hilbert phase (13), the switch-off/on can be read directly from the SSN record as indicated by the black crosses on Figure 1 (a) occurring respectively at approximately 1 year following the downcrossing, and at the upcrossing, by the 13 month smoothed SSN (Figure 1(a) red) of the 40 year smoothed SSN (Figure 1(a) blue) (38). The 40 year smoothed SSN tracks the Gleissberg cycle (26; 40).

Figure 1 (d) then points to a physical explanation of the empirical result obtained from constructing the solar clock (13): extreme geomagnetic storms ($aa > 300nT$) rarely occur within the quiet interval (grey shaded regions). Whilst the switch-on coincides with the termination of the extended cycle, the switch-off hitherto was only identified in a sharp overall reduction in extreme activity in the aa index, and other activity indicators (13; 41). A key result of this Letter is that the switch-off coincides with the ARs migrating to latitudes within approximately $\pm 15^\circ$ of the solar equator as can be seen in panels (b,c) of Figure 1. The switch-off then corresponds to the bands of ARs reaching the vicinity of the solar equator where the differential rotation is weakly varying so that the magnetic shearing driving CMEs is weaker. The switch-on coincides with the emergence of ARs at mid-latitudes where the differential rotation latitudinal gradient, and hence the magnetic shearing driving CMEs, is strong.

Mapping time to SSN Hilbert analytic phase (see Methods) allows us to overlay multiple cycles of activity on a single normalized cycle. This solar cycle clock is constructed in Figure 2. On the clock, the switch-off (green) and switch-on (red) bracket the $4\pi/5$ quiet interval centred on the average solar mininum. Daily exceedences in the full record of the aa index (over 14 solar cycles) are indicated by black 'spokes' and these show that extreme events in aa rarely occur in the quiet interval. The (unsigned) latitudes of bins containing AR areas $> 50\mu Hem$ for the full AR record (over 13 solar cycles) are shaded orange, latitude is plotted from zero at the centre of the clock, so that as time increases clockwise, the AR latitudes spiral inwards. The blue circle indicates unsigned latitude of 15°. The switch-off then coincides with almost all of the AR migrating to below 15° in latitude. The AR start to reappear at high latitudes around mininum, and progressively occupy lower latitudes thereafter, reaching 15° latitude around the switch-on.

The relationship between AR latitudes and geomagnetic activity is charted in more detail in Figure 3. The panels in Figure 3 plot the solar clock of Figure 2 unwrapped so that AR latitude is plotted versus solar cycle phase, with the averaged solar minimum at the centre of each panel (black vertical line) and the switch-off (green line) and switch-on (red line) at $-2\pi/5$ and $+2\pi/5$ respectively. All panels overplot for the full AR database (over 13 solar cycles) the latitude bins and Carrington rotations containing significant (ie $\geq 50\mu Hem$) AR areas in grey. Blue horizontal lines indicate $\pm 15^\circ$ latitude. The left-hand panels summarize the latitudinal extent of the ARs. Panels (a) and (c) plot the 13 Carrington rotation smoothed latitudes lower and upper boundaries, above (a) and below (c) which 90% of the AR area is found, and panel (e) plots the AR latitude centroid. For all 13 cycles of AR data, panel (c) shows that the switch-off marks the time when at least 90% of the AR have moved to within 15° of the equator . The switch-on coincides with

the AR extending from $\pm 15^\circ$ to higher latitudes, so that their low latitude boundary, the blue lines in panel (a) just extend to $\pm 15^\circ$,

The AR area data does not allow us to pin-point which sunspot group, recorded as a binned AR area, is the genesis of an extreme solar eruption. However we can for each Carrington rotation during which an extreme event is seen in the aa index indicate which latitude bins contain significant (ie $\geq 50 \mu Hem$) sunspot areas. This is shown in panels (b) and (d) which show that the more extreme events $aa > 300nT$ very rarely occur within the quiet interval. The extreme events switch-off when the ARs are within 15° of the equator. This can also be seen in each individual cycle which are plotted in Figure ED4. The extreme event switch-on is when the AR areas extend from $\pm 15^\circ$ to higher latitudes so that the most active, shear dominated latitudes are fully populated with sunspot activity.

If we attribute the switch off of the most extreme events seen in the aa index with sunspot AR areas moving to a region of reduced gradient in overall solar differential rotation, then this should mark the transition from shear dominated extreme events (CMEs) to high speed streams. This is shown in Figure 3 panel (f) which indicates the latitude bins containing significant AR areas during Carrington rotations where there is both extreme aa activity and significant 27 day autocovariance. This corotating high speed stream associated activity is first seen when the sunspot centroids (panel (e)) move to within 15° of the equator, so that the AR areas are spanning $\pm 15^\circ$ (see also the individual cycles plotted in Figure ED4). It corresponds to an interval of more moderate events, aa typically less than $300nT$ which occurs before, and overlaps with, the switch-off and continues until solar miminum, when ARs start to reappear at high latitudes.

Although the AR appear in a highly intermittent manner, when their overall latitudinal path is tracked, it forms part of an extended cycle of activity (42; 43) which commences at high latitudes and terminates at the equator (35). The extended cycle latitudinal bands can be identified in multiple features of activity ((43; 44) and refs. therein). However, a simple model for the track of the extended cycle latitudes can be obtained solely from the AR timeseries (see Methods) and this is plotted with black dashed lines on all panels of Figure 3. The simple model is obtained from fitting a linear relationship between AR area centroid latitudes seen in the more active half of the cycle, and Hilbert phase. This extrapolates to zero latitude approximately at the switch-on, so that it roughly coincides with the average of terminator times that have been directly identified as the time when EUV bright point annihilate at the equator (37). The AR area latitudes for the active sun then directly relate to/predict the cycle termination and birth of the new cycle. The extended cycle track crosses $\pm 15^\circ$ latitude at phase $\pm \pi$, that is, half a normalized Schwabe cycle in advance of/following solar minimum (which is not at solar maximum, see Figure 2).

Extreme space storms are rare, so that statistical quantification of the solar cycle variation of their occurrence probability is challenging (45). It is intimately related to a quantitative understanding of the solar cycle of activity. The Hilbert transform of the 13 month smoothed SSN can be used to map the variable length Schwabe cycle of activity onto a uniform clock. This reveals a clear correspondence between active region latitudes and both the level, and class, of extreme geomagnetic activity at earth. Although

it is well understood that there is an overall relationship between the butterfly pattern of sunspot activity with solar latitude, the SSN, and geomagnetic activity at earth, the solar cycle clock pin-points the phase in the cycle when the most extreme, CME driven events are switched-off as their potential AR area sources move to within about 15° of the equator, where the latitudinal gradient in differential rotation is reduced. This overlaps with the onset of more moderate events that are coincident with 27 day recurrences in the *aa* index, consistent with high-speed streams. This directly relates the latitude of the sunspot ARs, and the track of the extended solar cycle, with the longstanding identification by (14) (see also (15; 46)) of a two-component cycle of geomagnetic activity with two different sources—one due to solar activity (flares, CMEs, and filament eruptions) that follows the sunspot cycle and another due to recurrent high speed solar wind streams that peaks during the decline of each cycle.

The pattern of activity revealed by the solar cycle clock provides a metric for systematic comparison with dynamo theories of the solar cycle. Model predictions of SSN can be translated into a clock which specifies the corresponding AR overall latitudes and the track of the extended cycle. Given that Feynman's interplanetary component of the *aa* index is a good predictor of the strength of the following solar cycle (14; 15), using the clock to organise model-data comparison may also inform solar cycle prediction.

2 Methods

2.1 Construction of the solar clock

The analytic signal (47; 48) $A(t)exp[i\phi(t)] = S(t) + iH(t)$ with time-varying amplitude $A(t)$ and phase $\phi(t)$ was obtained for the monthly total sunspot number (SSN) time series $S(t)$ and its Hilbert transform $H(t)$. This provides a mapping between time and signal phase, converting the (variable) duration of each solar cycle into a corresponding uniform phase interval, from 0 to 2π. A standard method was used to obtain the discrete analytic signal (49) which satisfies both invertability and orthogonality. The analytic signal will only be physically meaningful if the instantaneous frequency $\omega(t) = d\phi(t)/dt$ remains positive (48). This is ensured by removing both fast fluctuations and a slow trend before performing the Hilbert transform (see e.g. Chapman et al. (13); Boashash (48)). The slow trend was obtained by a robust local linear regression of the monthly SSN which down-weights outliers ('rlowess') using a 40 year window, which essentially obtains the Gleissberg cycle ((26)). The Hilbert transform was the performed on a 13 month moving average of the SSN, with this slow trend subtracted, as detailed in Figure ED1. The absolute signal phase is arbitrary and here is set to zero at the average of the phases of the SILSO mimima of cycles 1-25. The location of the switch-off and on are then set at phases $\pm 2\pi/5$ either side of zero. The switch-on closely coincides with the average phase of the last 12 terminators (37), which occurs 0.054 radians or ~ 1.13 (normalized to an 11 year cycle) months later.

2.2 Accuracy of the clock

This analysis is based on relative occurrence times between the AR areas and *aa* index records. Timings have been compared via the Hilbert transform phase obtained from the monthly SSN record. The accuracy of these comparisons is then limited by the time resolution of the data records and quantities extracted from them. The AR areas are reported per Carrington rotation. The *aa* index is of 3 hour time resolution, and to compare the amplitude of events, we identify the central time of the Carrington rotations during which *aa* exceeds a threshold value of $100 - 600nT$. To compare 27 day recurrences, we identify the central time of the Carrington rotations during which the 27 day lagged autocovariance of the *aa* index exceeds 0.25, the autocovariance is estimated over 100 day window. The clock phase zero is set at the occurrence of the average of the last 25 solar minima as times by SILSO, the individual SILSO minima have a STD of 0.3 radians in phase, or 0.5 normalized years, about this value. The switch-on and off are directly related to the averaged mimumum. The switch-on closely coincides with the average phase of the last 12 terminators (37), which occurs 0.054 radians or ~ 1.13 (normalized to an 11 year cycle) months later. The individual terminators also have inter-cycle variability and a Hale cycle dependence (26), so that we do not use their Schwabe cycle average to directly determine the switch-off/on. The stability of absolute clock timings against variation in the choice of smoothing window for the Hilbert transform have been investigated previously (13; 50).

2.3 Extended cycle.

A simple model for the latitude of the extended cycle is obtained from the AR centroids as shown in Figure ED3. The Figure plots the AR centroid latitude θ at the Hilbert phase ϕ at the mid point of each Carrington rotation (black points). The AR centroids from multiple solar cycles can be seen to fall on a single path in latitude and phase, recovering the result of (51) that required detailed parametric fitting to the shape of the AR latitude timeseries. A linear least squares regression is obtained for the AR centroids for the most active half of the (normalized) cycle, from the switch on at $+2\pi/5$ to half a cycle later at $2\pi/5 + \pi$ (overplotted blue points). This avoids fitting to lower latitudes where there is a zone of avoidance known as Spörer's law of zones (4). The fitted line (red) is $\theta = a(\phi - b)$ with $a = -3.214$ and $b = 7.684$. This fitted line is then extrapolated to give an extended cycle latitude centroid, shown by repeating the AR centroids over a second interval of 2π in phase (grey points). The simple model extended cycle terminates (intersects zero latitude) approximately at the switch-on, $2\pi/5$ phase.

2.4 Differential rotation

Using the 'standard' differential rotation curve (20) for the differential rotation at latitude ϕ of $2.90 - 0.35[sin^2\phi + sin^4\phi\ \mu Rads^{-1}$, the differential rotation changes by about 13 % between the equator and 15° latitude.

2.5 Identifying 27 day recurrence in the *aa* index

Sargent (23, 24) originally obtained the cross correlation coefficients between successive 27 day intervals of the *aa* index (11; 16) and then performed truncation and smoothing to produce the original R27 index. Here the autocovariance of the *aa* index is used directly as in (26). For a real-valued discrete signal x_i the raw (R_m) and normalized ($acv(m)$) covariance (52) of a sequence with itself (i.e. the "autocovariance") as a function of lag m is, for $m \geq 0$:

$$R_m = \sum_{n=0}^{W-m-1} \left(x_{n+m} - \frac{1}{W} \sum_{i=0}^{W-1} x_i \right) \left(x_n - \frac{1}{W} \sum_{i=0}^{W-1} x_i \right) \quad (1)$$

$$acv(m) = \frac{R_m}{R_0} \quad (2)$$

with the symmetry property that for $m < 0$, $acv(m) = acv(-m)$. In the above, the autocovariance is obtained for the sample window $i = 1 \ldots W$ of the x_i. The autocovariance of the full resolution *aa* index is calculated at all lags m for a $W = 100$, 100 day window centred on each day of the record. The 27 day recurrence is considered significant if it exceeds a threshold of 0.25 as this is significantly above the level seen at other lags where recurrence is not expected (10 day lag is plotted in Figure 2 for comparison). Figure 3(f) then plots all Carrington rotations within which R(27days) both exceeds the threshold of 0.25 and the *aa* exceeds a threshold [100 200 300 400 500 600] used throughout.

3 Data Availability

All data used in this study is freely available from the following sources (accessed on 1st October 2023).

SILSO Royal Observatory of Belgium, Brussels monthly total sunspot number version 2.0 from 1749: http://www.sidc.be/silso/home

The dates of solar cycle maxima and minima are as determined from the smoothed sunspot number record by SILSO: http://www.sidc.be/silso/cyclesmm

The Active Region areas record reports total sunspot area (in units of millionths of a hemisphere) found in 50 latitude bins distributed uniformly in Sine(latitude) per Carrington rotation since 1874, available from: http://solarcyclescience.com/AR_Database/bflydata.txt

The 3 hour time resolution *aa* index dataset since 1868 is available from the International Service of Geomagnetic Indices at http://isgi.unistra.fr/

The solar radio flux at 10.7 cm (the F10.7 index) is available since 1947 at:

https://www.spaceweather.gc.ca/solarflux/sx-en.php

Supplementary information. Extended Data is appended to this preprint.

Acknowledgments. SCC acknowledges support from ISSI via the J. Geiss fellowship and AFOSR grant FA8655-22-1-7056 and STFC grant ST/T000252/1. TD acknowledges support from CNES.

Declarations

- Funding AFOSR grant FA8655-22-1-7056
- Conflict of interest: none
- Ethics approval: not applicable
- Consent to participate: not applicable
- Consent for publication: not applicable
- Availability of data and materials: all data avaiable online, see data availability statement
- Code availability: standard Matlab packages used, code available on request.
- Authors' contributions: SCC devised and performed the analysis, all authors contributed to the manuscript.

4 Extended Data

Figures are as follows:

1. **Figure ED1**: Shows the procedure for performing the Hilbert transform of the SSN record to construct the solar cycle clock, and how the quiet intervals are identified.
2. **Figure ED2**: The AR butterfly diagram of sunspot active region areas versus latitude, areas colour-coded with the occurrence of space weather extreme events.
3. **Figure ED3**: A simple model for the extended cycle path in latitude versus phase of the clock, obtained from the AR latitude centroids.
4. **Figure ED4**: Sunspot AR latitudes colour-coded with extreme and recurrent geomagnetic activity plotted versus time for the last 13 solar cycles. These are overplotted with the latitudes of the upper bound, and the centroid, latitudes of the AR areas, to provide a time-unfolded version of Figure 3 main paper.

References

[1] Hapgood, M. (2019). The great storm of May 1921: An exemplar of a dangerous space weather event. Space Weather, 17, 950–975.

[2] Oughton et al (2017), Quantifying the daily economic impact of extreme space weather due to failure in electricity transmission infrastructure, Space Weather,15,65–83

[3] Knipp, D. J., Bernstein, V., Wahl, K., Hayakawa, H., (2021) Timelines as a tool for learning about space weather storms J. Space Weather Space Clim. 11, 29 doi:10.1051/swsc/2021011

[4] Hathaway, D. H., (2015) The solar cycle, Living Rev. Solar Phys., 12, 4 doi:10.1007/lrsp-2015-4

[5] Baker, D. N., Lanzerotti, L. J., Resource Letter SW1: Space weather, Am. J. Phys. 84, 166 (2016) doi:10.1119/1.4938403

[6] Yermolaev, Y. I., Lodkina, I. G., Nikolaeva, N. S. and Yermolaev, M. Y. (2013). Occurrence rate of extreme magnetic storms, J. Geophys. Res. Space Physics, 118, 4760–4765, doi:10.1002/jgra.50467.

[7] Pulkkinen, T. Space Weather: Terrestrial Perspective. Living Rev. Sol. Phys. 4, 1 (2007) doi:10.12942/lrsp-2007-1

[8] Baker, D. N., X Li, A. Pulkkinen, C. M. Ngwira, M. L Mays, A. B. Galvin, and K. D. C. Simunac (2013), A major solar eruptive event in July 2012: Defining extreme space weather scenarios, Space Weather, 11, 585-591, doi:10.1002/swe.20097.

[9] Hayakawa, H., Ribeiro, P., Vaquero, J. M., Gallego, M. C., Knipp, D. J., Mekhaldi, F., Bhaskar, A., Oliveira, D. M., Notsu, Y., Carrasco, V. M. S., Caccavari, A., Veenadhari, B., Mukherjee, S., and Ebihara, Y., (2020) The Extreme Space Weather Event in 1903 October/November:An Outburst from the Quiet Sun, The Astrophysical Journal Letters, doi:10.3847/2041-8213/ab6a18

[10] Charbonneau, P., Sokoloff, D. Evolution of Solar and Stellar Dynamo Theory. Space Sci Rev 219, 35 (2023). doi:10.1007/s11214-023-00980-0

[11] Mayaud, P-N. (1972) The aa indices: A 100 year series characterizing the magnetic activity, J. Geophys. Res., 77, 6870

[12] Lockwood M., Owens, M. J., Barnard, L. A., Scott, C. J., Watt, C. E., Bentley, S., (2018) Space climate and space weather over the past 400 years: 2. Proxy indicators of geomagnetic storm and substorm occurrence,J. Space Weather Space Clim., 8, A12 doi:10.1051/swsc/2017048

[13] S. C. Chapman, S. W. McIntosh, R. J. Leamon, N. W. Watkins, Quantifying the solar cycle modulation of extreme space weather, Geophysical Research Letters, (2020) doi:10.1029/2020GL087795

[14] Feynman, J., Geomagnetic and solar wind cycles 1900-1975, 87, 6153 JGR (1982)

[15] D.H. Hathaway, R.M. Wilson (2006) Geomagnetic activity indicates large amplitude for sunspot cycle 24. Geophys. Res. Lett. 33, L18101 doi: 10.1029/2006GL027053

[16] Mayaud, P. N. (1980). Derivation, Meaning, and Use of Geomagnetic Indices, Geophys. Monogr. Ser., vol. 22, AGU, Washington, D.C. doi:10.1029/GM022

[17] Chapman S. C., Horne, R. B., Watkins, N. W. (2020a) Using the *aa* index over the last 14 solar cycles to characterize extreme geomagnetic activity, Geophys. Res. Lett, doi: 10.1029/2019GL086524

[18] S. C. Chapman, N. W. Watkins, E. Tindale, (2018)Reproducible aspects of the climate of space weather over the last five solar cycles, Space Weather, DOI:10.1029/2018SW001884

[19] Bergin, A., S. C. Chapman, N. Moloney, N. W. Watkins (2022) Variation of geomagnetic index empirical distribution and burst statistics across successive solar cycles, J. Geophys. Res, doi:10.1029/2021JA029986

[20] Beck JG (2000) A comparison of differential rotation measurements - (invited review). Sol Phys 191(1):47–70. doi:10.1023/A:1005226402796

[21] D. J. McComas, H. A. Elliott, N. A. Schwadron, J. T. Gosling, R. M. Skoug, B. E. Goldstein (2003) The three-dimensional solar wind around solar maximum GRL doi:10.1029/2003GL017136

[22] Luhmann, J.G., Lee, C.O., Li, Y. et al. Solar Wind Sources in the Late Declining Phase of Cycle 23: Effects of the Weak Solar Polar Field on High Speed Streams. Sol Phys 256, 285–305 (2009). doi:10.1007/s11207-009-9354-5

[23] Sargent, H. H., (1985) Recurrent geomagnetic activity evidence for long-lived stability in solar wind structure J. Geophys. Res. 90, A2, 1425-1428

[24] Sargent, H. H., (2021) A revised 27 day recurrence index, arXiv:2101.02155 [astro-ph.SR]

[25] Tsurutani, B. T., et al. (2006) Corotating solar wind streams and recurrent geomagnetic activity: A review, J. Geophys. Res., 111, A07S01, doi:10.1029/2005JA011273.

[26] S. C. Chapman, S. W. McIntosh, R. J. Leamon, N. W. Watkins, The Sun's magnetic (Hale) cycle and 27 day recurrences in the aa geomagnetic index. Ap. J. (2021) doi: 10.3847/1538-4357/ac069e

[27] Stansby, D., Green, L.M., van Driel-Gesztelyi, L. et al. Active Region Contributions to the Solar Wind over Multiple Solar Cycles. Sol Phys 296, 116 (2021). https://doi.org/10.1007/s11207-021-01861-x

[28] Forbes, T.G., Linker, J.A., Chen, J. et al. CME Theory and Models. Space Sci Rev 123, 251–302 (2006). https://doi.org/10.1007/s11214-006-9019-8

[29] Webb, D.F., Howard, T.A. Coronal Mass Ejections: Observations. Living Rev. Sol. Phys. 9, 3 (2012). https://doi.org/10.12942/lrsp-2012-3

[30] Chen, P.F. Coronal Mass Ejections: Models and Their Observational Basis. Living Rev. Sol. Phys. 8, 1 (2011). https://doi.org/10.12942/lrsp-2011-1

[31] Hathaway, D. H., L. A. Upton, S. S. Mahajan (2022) Variations in differential rotation and meridional flow within the Sun's surface shear layer 1996–2022. Frontiers in Astronomy and Space Sciences, 9, 1007290. doi:10.3389/fspas.2022.1007290

[32] Norton, A., Howe, R., Upton, L. et al. Solar Cycle Observations. Space Sci Rev 219, 64 (2023). doi:10.1007/s11214-023-01008-3

[33] Vourlidas, A., Howard, R.A., Esfandiari, E., Patsourakos, S., Yashiro, S. and Michalek, G., (2010), Comprehensive analysis of coronal mass ejection mass and energy properties over a full solar cycle Astrophys. J., 722, 1522–1538.DOI 10.1088/0004-637X/722/2/1522

[34] Owens, M. J., M. Lockwood, L. Barnard, C. J. Davis (2011) Solar cycle 24: Implications for energetic particles and long-term space climate change, Geophys. Res. Lett., L19106, doi:10.1029/2011GL049328

[35] McIntosh, S.W., Leamon, R.J. (2014 a) On Magnetic Activity Band Overlap, Interaction, and the Formation of Complex Solar Active Regions. Astrophys. J. Lett. 796, L19

[36] McIntosh, S.W., Wang, X., Leamon, R.J., Scherrer, P.H.: (2014 b) Identifying Potential Markers of the Sun's Giant Convective Scale. Astrophys. J. Lett. 784, L32.

[37] McIntosh, S.W., Leamon, R.J., Egeland, R., Dikpati, M., Fan, Y., Rempel, M. (2019), What the sudden death of solar cycles can tell us about the nature of the solar interior. Solar Physics 294 (7), 88. doi:10.1007/s11207-019-1474

[38] S. C. Chapman, Charting the Solar Cycle, Front. Astron. Space Sci. - Space Physics, (2023) doi: 10.3389/fspas.2022.1037096

[39] Cliver, E. W., Svalgaard, L. (2004) The 1859 Solar-terrestrial disturbance and the current limits of extreme space weather activity Solar Physics 224: 407-422

[40] Gleissberg, W., Secularly smoothed data on the minima and maxima of sunspot frequency, (1967) Solar Phys. 2, 231

[41] Leamon, R.J., McIntosh, S.W., Title, A.M (2022) Deciphering solar magnetic activity, the solar cycle clock, Front. Astron. Space Sci. 9:886670. doi: 10.3389/fspas.2022.886670

[42] R. P. Wilson, R. C. Altrock, K. L, Harvey, S. F. Martin, H. B. Snodgrass, (1988) The extended solar activity cycle, Nature, 333, 748

[43] Cliver, E. W. (2014). The extended cycle of solar activity and the Sun's 22-Year magnetic cycle. Space Sci. Rev. 186, 169–189. doi: 10.1007/s11214-014-0093-z

[44] McIntosh, S.W., Leamon, R.J., Egeland, R. et al. Deciphering Solar Magnetic Activity: 140 Years of the 'Extended Solar Cycle' – Mapping the Hale Cycle. Sol Phys 296, 189 (2021). doi:10.1007/s11207-021-01938-7

[45] Riley, P., Love, J. J., (2016) Extreme geomagnetic storms: Probabilistic forecasts and their uncertainties, Space Weather, 15, 53–64, doi:10.1002/2016SW001470.

[46] Legrand, J.P., Simon, (1991) P.A. A two-component solar cycle. Sol Phys 131, 187–209 doi:10.1007/BF00151753

[47] Gabor, D. "Theory of Communication." J. IEE (London). Vol. 93(3), 1946, pp. 429-441.

[48] Boashash, B. Estimating and Interpreting the Instantaneous Frequency of a Signal. Proc. IEEE®. Vol. 80(4), 1992, pp. 520-568.

[49] Marple, S. L. (1999) "Computing the Discrete-Time Analytic Signal via FFT." IEEE® Transactions on Signal Processing. Vol. 47, , pp. 2600–2603.

[50] McIntosh, S.W., Chapman, S., Leamon, R.J. et al. (2020) Overlapping Magnetic Activity Cycles and the Sunspot Number: Forecasting Sunspot Cycle 25 Amplitude. Sol Phys 295, 163 doi: 10.1007/s11207-020-01723-y

[51] Hathaway, D.H. A Standard Law for the Equatorward Drift of the Sunspot Zones. Sol Phys 273, 221–230 (2011). doi: 10.1007/s11207-011-9837-z

[52] Bendat, J.S., Piersol, A.G. (2010) Random Data: Analysis and Measurement Procedures. 4th Edition. Wiley.

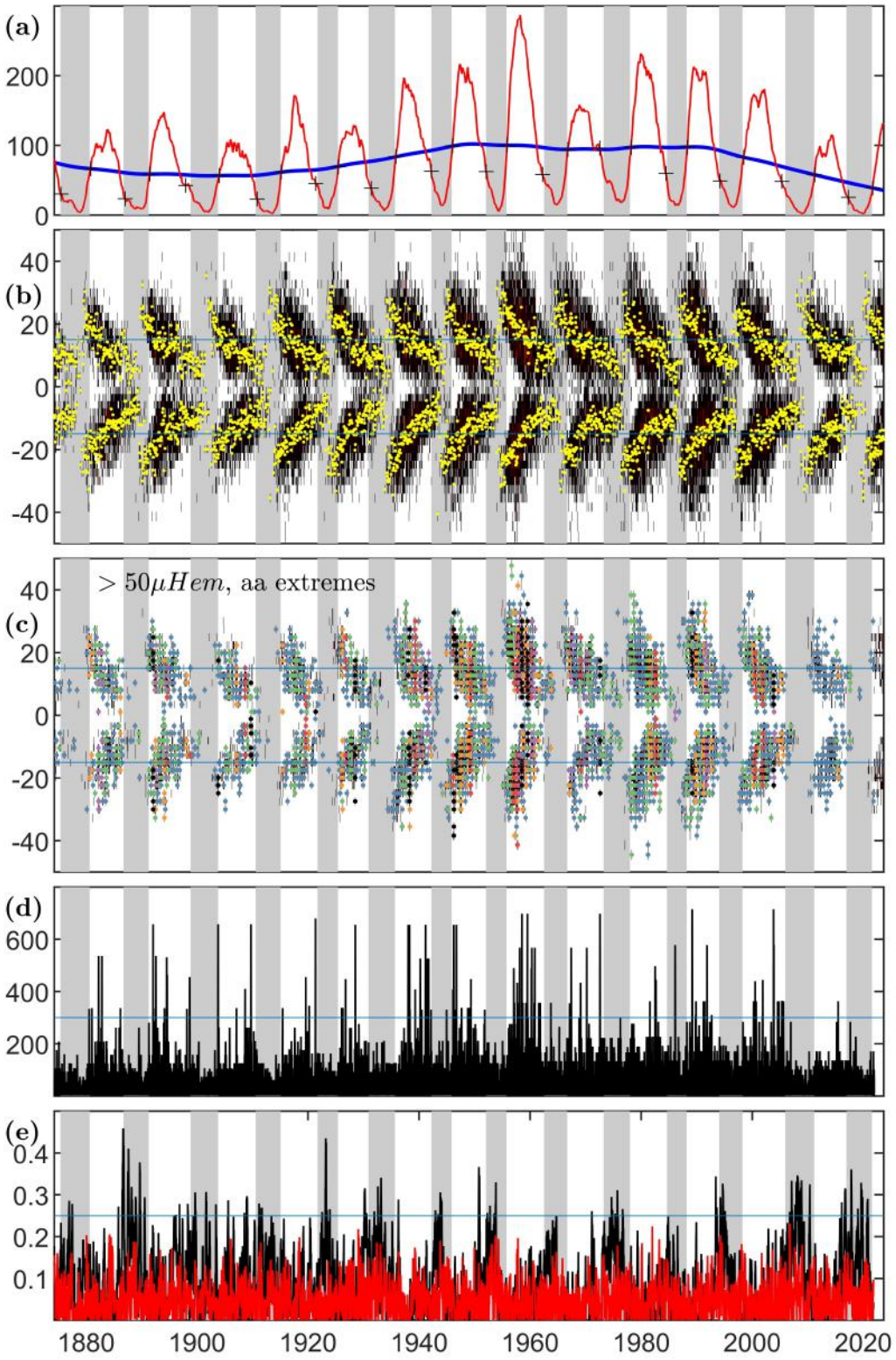

Fig. 1 Time evolution of sunspot number, area latitudes and extreme and recurrent geomagnetic activity. Grey shading indicates the quiet interval between switch-off and switch-on on all panels. Panel (a): 13 month smoothed SSN (red) and 40 year smoothed SSN (blue). Black crosses are at times 12 months following the smoothed SSN downcrossing of the 40 year smoothed SSN, and at the smoothed SSN upcrossing of the slow trend, providing estimates of the switch-off and switch-on times respectively. Panel (b): active region areas in single Carrington rotation-latitude bins (black) overplotted with the area centroid for each Carrington rotation (yellow). Panel (c) overplots on all sunspot area latitude bins with area $> 50\mu Hem$ the Carrington rotation during which the *aa* index exceeds a threshold of 100 (blue) 200 (green) 300 (orange) 400 (red) 500 (purple) 600 (black) nT. Horizontal blue lines on panels (b.c) indicate latitudes $\pm 15°$. Panel (d): the *aa* geomagnetic index, blue line indicates $aa = 300nT$. Panel (e) *aa* index autocovariance at a lag of 27 days, approximately the solar rotation (black) and at 10 days (red), to provide an indication of the level of 'by chance' autocovariance, this is exceeded by the horizontal blue line at 0.25.

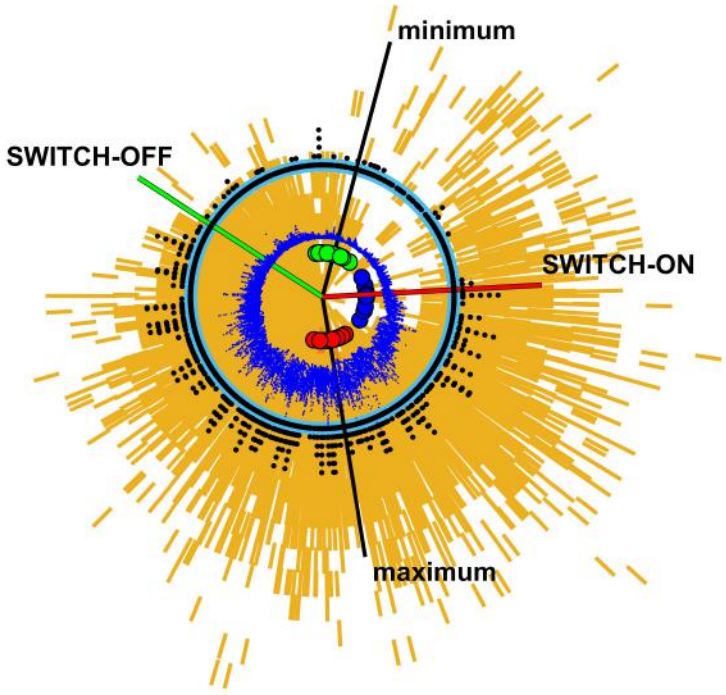

Fig. 2 Clock of regular 11 year cycle showing area latitudes and extreme geomagnetic activity. Solar cycle clock constructed such that increasing time (analytic phase) is read clockwise. The analytic phases of the maxima and minima are indicated by red and green circles respectively and the blue circles indicate terminators identified by (37). Black lines indicate the average analytic phase for the 25 cycle average maxima and minima. The switch-off (green line) and on (red line) are at $\pm 2\pi/5$ in phase either side of the 25 solar cycle average minimum phase. Black dots arranged on concentric circles where increasing radius indicates *aa* values which in any given day exceeded $100, 200, 300, 400, 500, 600nT$. Blue dots overplot daily F10.7. Orange overplots all unsigned latitude bins containing AR areas exceeding $50\mu Hem$ with zero latitude at the clock centre and 15° latitude marked by the blue circle.

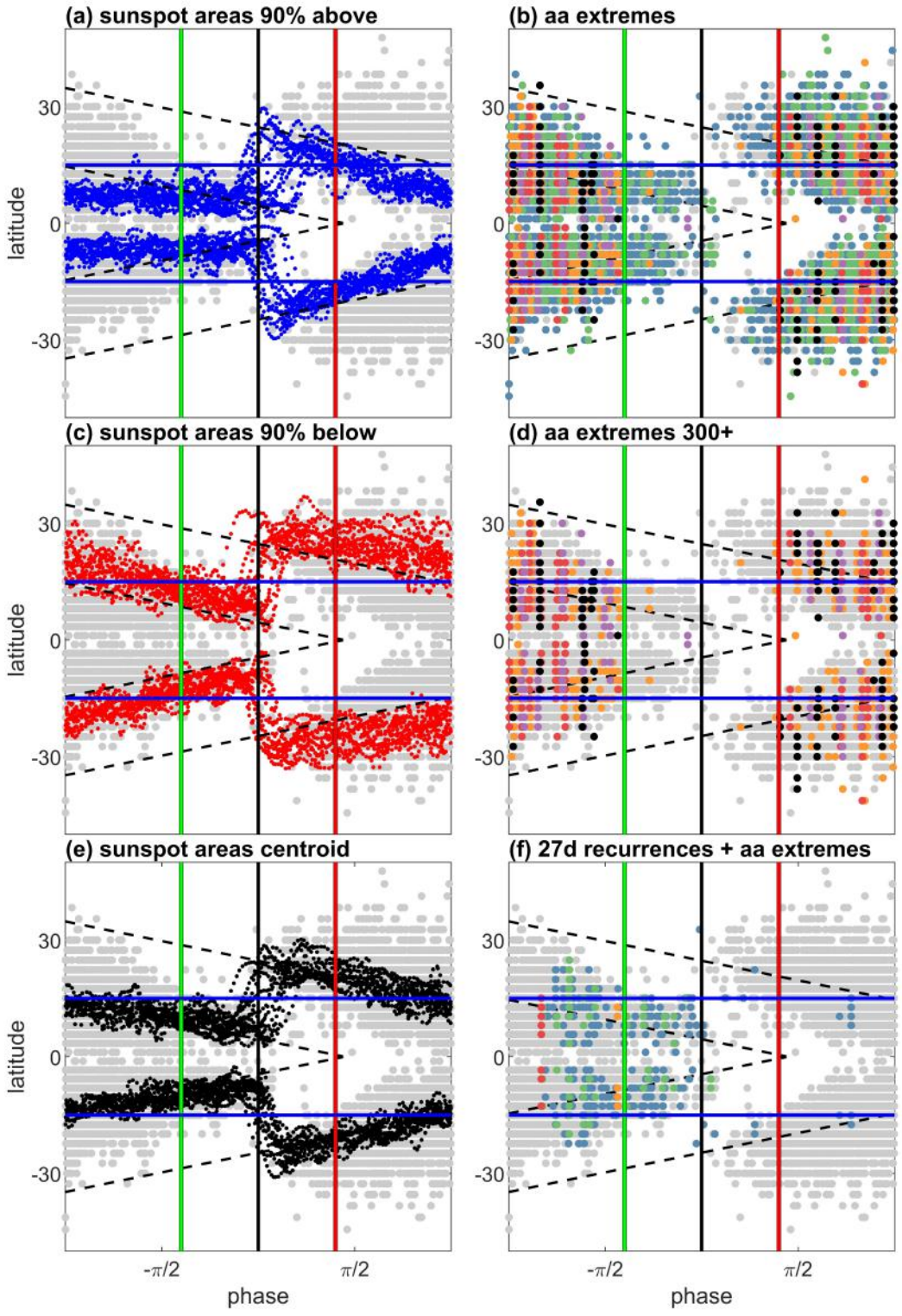

Fig. 3 Active region area latitudes and extreme and recurrent geomagnetic activity overplotted for the last 13 solar cycles. All panels: latitude plotted as a function of Hilbert phase of the SSN record (see Methods), grey circles plot centres of latitude bins for each Carrington rotation containing total AR area exceeding $50\mu Hem$, horizontal blue lines indicate $\pm 15^\circ$ latitude. The 25 cycle averaged minimum (black vertical line) is at phase zero and the switch-off (green line) and on (red line) are at phase $\pm\frac{2\pi}{5}$ either side. Black dashed lines plot the extended cycle estimated from AR latitude centroids (see Methods). Left panels: Lines plot 13 Carrington rotation smoothed latitudes which are the low latitude envelope (90% of total AR area are at higher latitudes, Panel a, blue) and the high latitude envelope (90% of total AR area are at lower latitudes, panel c, red) and AR area centroid (panel e, black). Right Panels: Panel (b) overplots on all AR area latitude bins with area $> 50\mu Hem$ the phase of the Carrington rotation during which the *aa* index exceeds a threshold of 100 (blue) 200 (green) 300 (orange) 400 (red) 500 (purple) 600 (black) nT. Panel (d) as for panel (b), for *aa* index exceeding 300 400 500 600 nT. Panel (f) as for panel (b) for Carrington rotations where the *aa* index both exceeds the $[100 - 600nT]$ threshold and has a 27 day lag autocovariance exceeding 0.25.

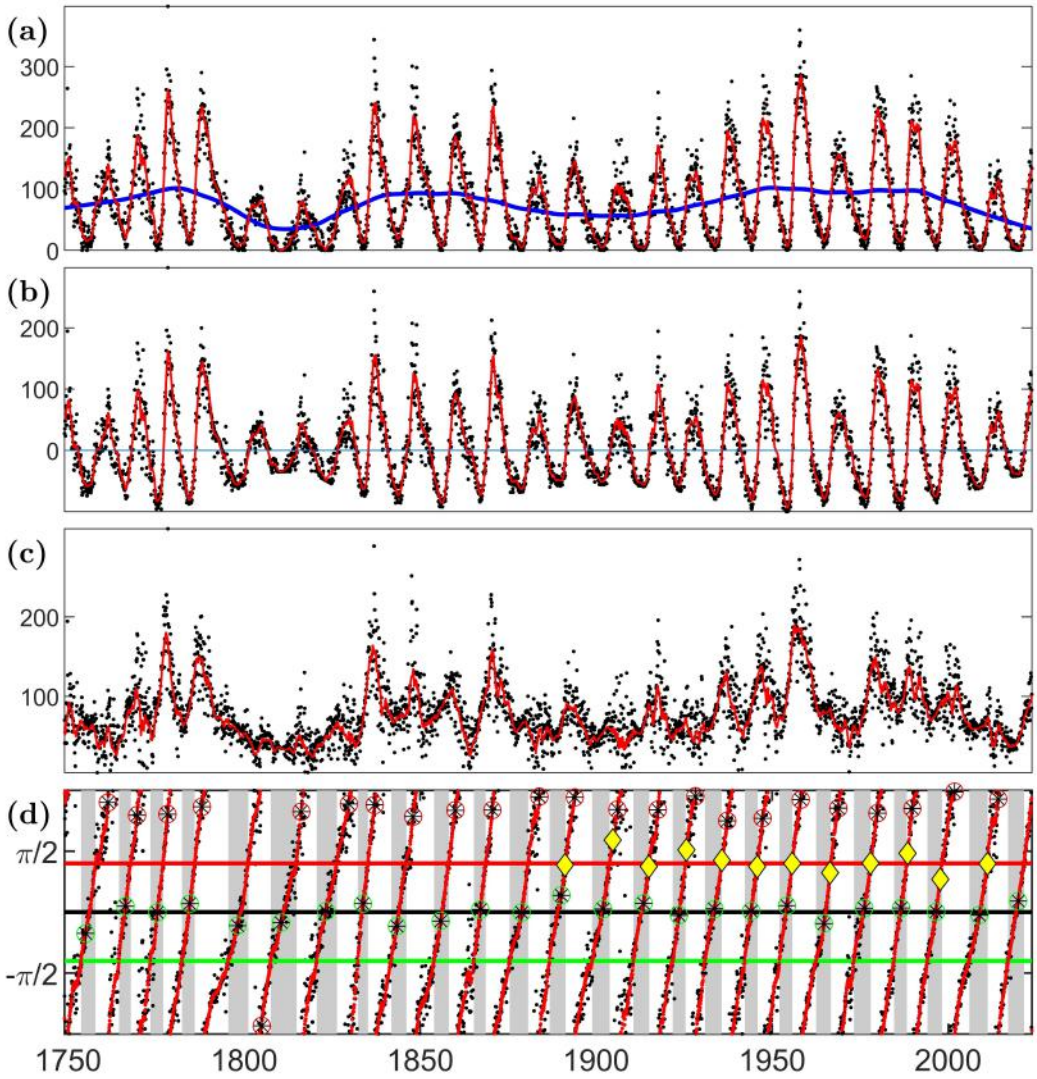

Extended Data 1 Constructing the solar clock and identifying the quiet intervals of the solar cycle. The Figure shows the procedure for performing the Hilbert transform of the SSN record. Panel (a): the monthly SSN (black dots), its 13 month running mean (red) and 40 year rlowess slow trend (blue). Panel (b) Monthly SSN and its 13 month running mean with slow trend subtracted. The time traces in panel (b) are Hilbert transformed and the analytic amplitude and phase are plotted in panels (c) and (d) respectively. Panel (d): the solar cycle maxima and minima (catalogued by SILSO) are indicated by red and green circled black asterisks respectively. Zero phase is set at the average phase of the minima of cycles 1-25. Yellow diamonds indicate terminators determined by (37). The switch-off (green line) and on (red line) are at phases $\pm 2\pi/5$ either side of the averaged minimum. The switch-off and switch-on phases then map to switch-off and switch-on times for each solar cycle which define the quiet intervals of each cycle (grey shading).

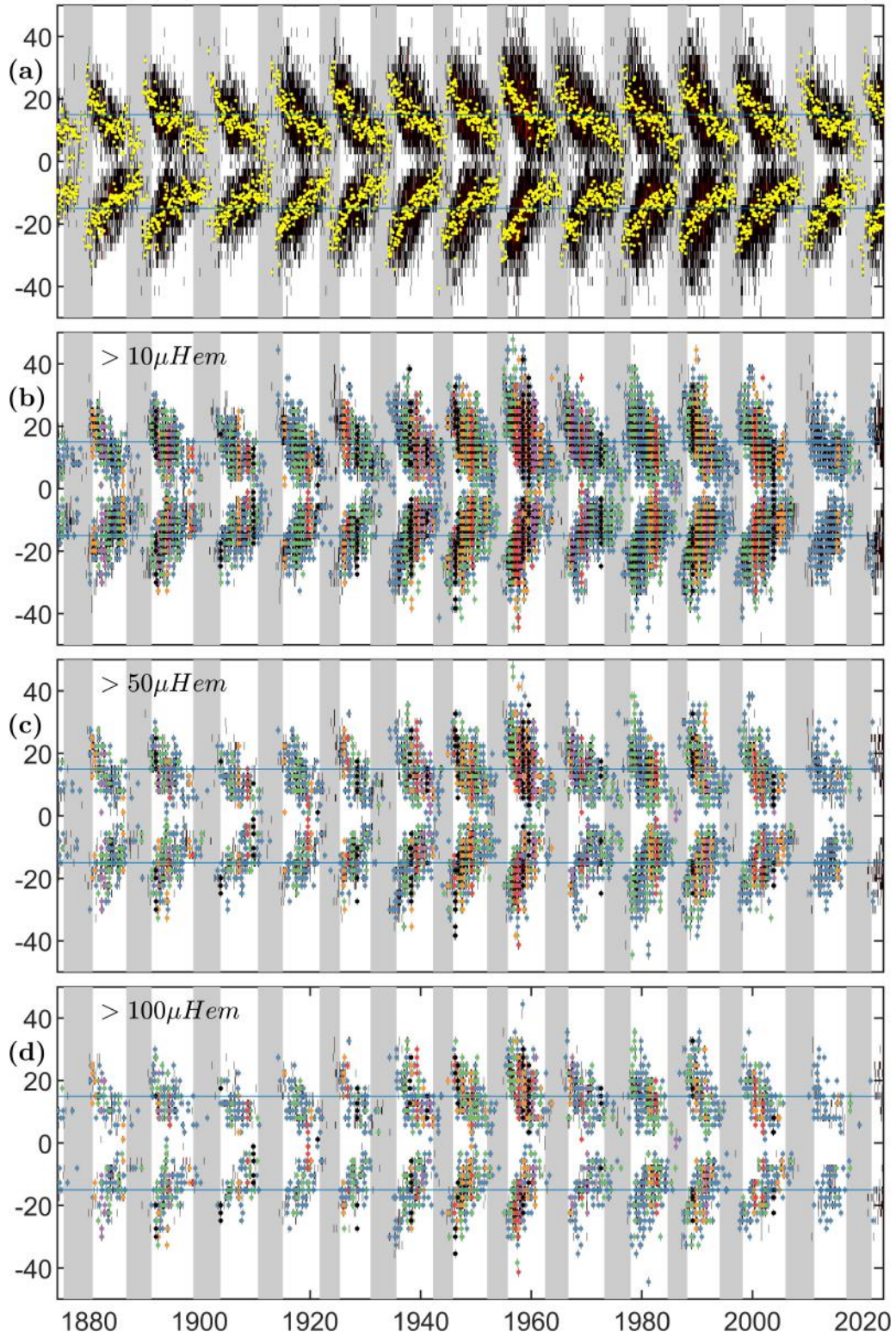

Extended Data 2 Butterfly diagram of sunspot areas colour-coded with space weather extreme events. Panel (a): total sunspot area (in units of millionths of a hemisphere, μHem) found in 50 latitude bins distributed uniformly in Sine(latitude) per Carrington rotation, overlotted (yellow) the area centroid for each Carrington rotation. Panels (b-d) plot total sunspot areas in bins where the area exceeds 10, 50 and 100 μHem respectively, overplotted are these bins colour-coded when the *aa* geomagntic index exceeds a threshold of 100 (blue) 200 (green) 300 (orange) 400 (red) 500 (purple) 600 (black) nT. Horizontal blue lines indicate latitudes $\pm 15°$.

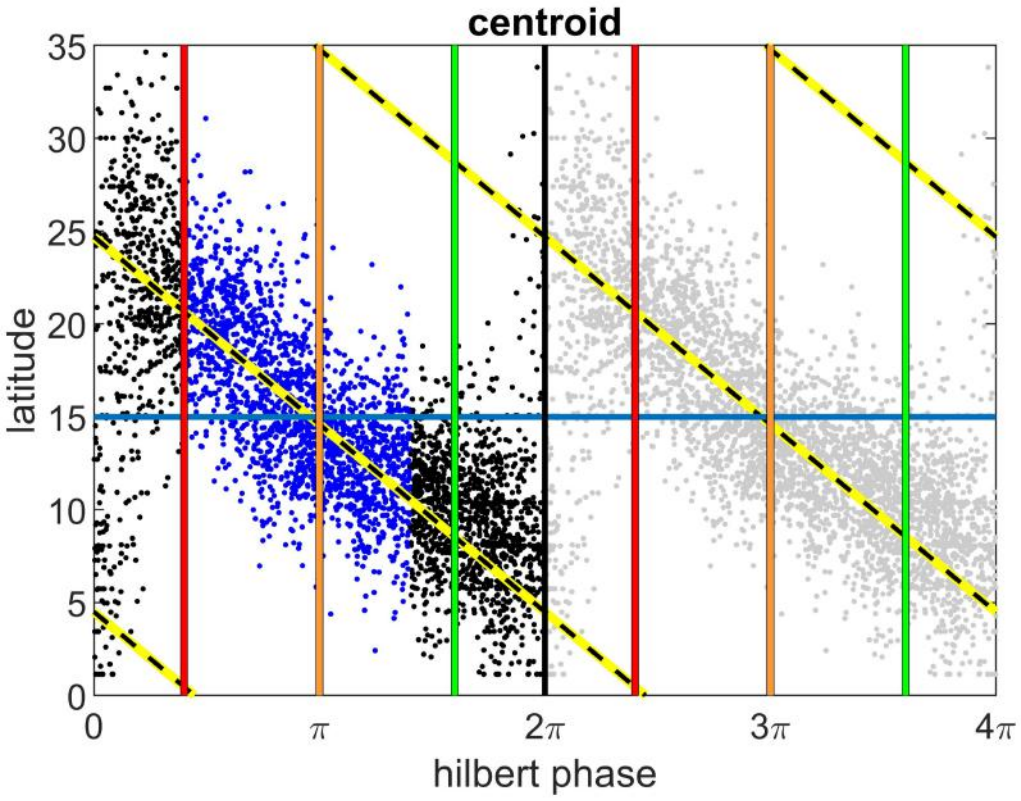

Extended Data 3 Simple model for the extended cycle. A simple model for the latitude of the extended cycle is obtained from the AR centroids. The Figure plots the AR centroid latitude θ at the Hilbert phase ϕ at the mid point of each Carrington rotation (black points). The model parameters are obtained from the linear least squares regression for the most active half of the (normalized) cycle, from the switch on at $+2\pi/5$ to half a cycle later at $2\pi/5 + \pi$ (overplotted blue points). The resulting fit (yellow highlighed black dashed lines) is $\theta = a(\phi - b)$ with $a = -3.214$ and $b = 7.684$, it is extrapolated to model the extended cycle, shown by repeating the AR centroids over a second interval of 2π in phase (grey points). The simple model extended cycle terminates (intersects zero latitude) approximately at the switch-on, $2\pi/5$ phase, and crosses 15° latitude at π phase (horizontal blue line). The switch-on and off are indicated by vertical red and green lines respectively, the plot is centred on the average minimum which is at zero (2π) phase (black line).

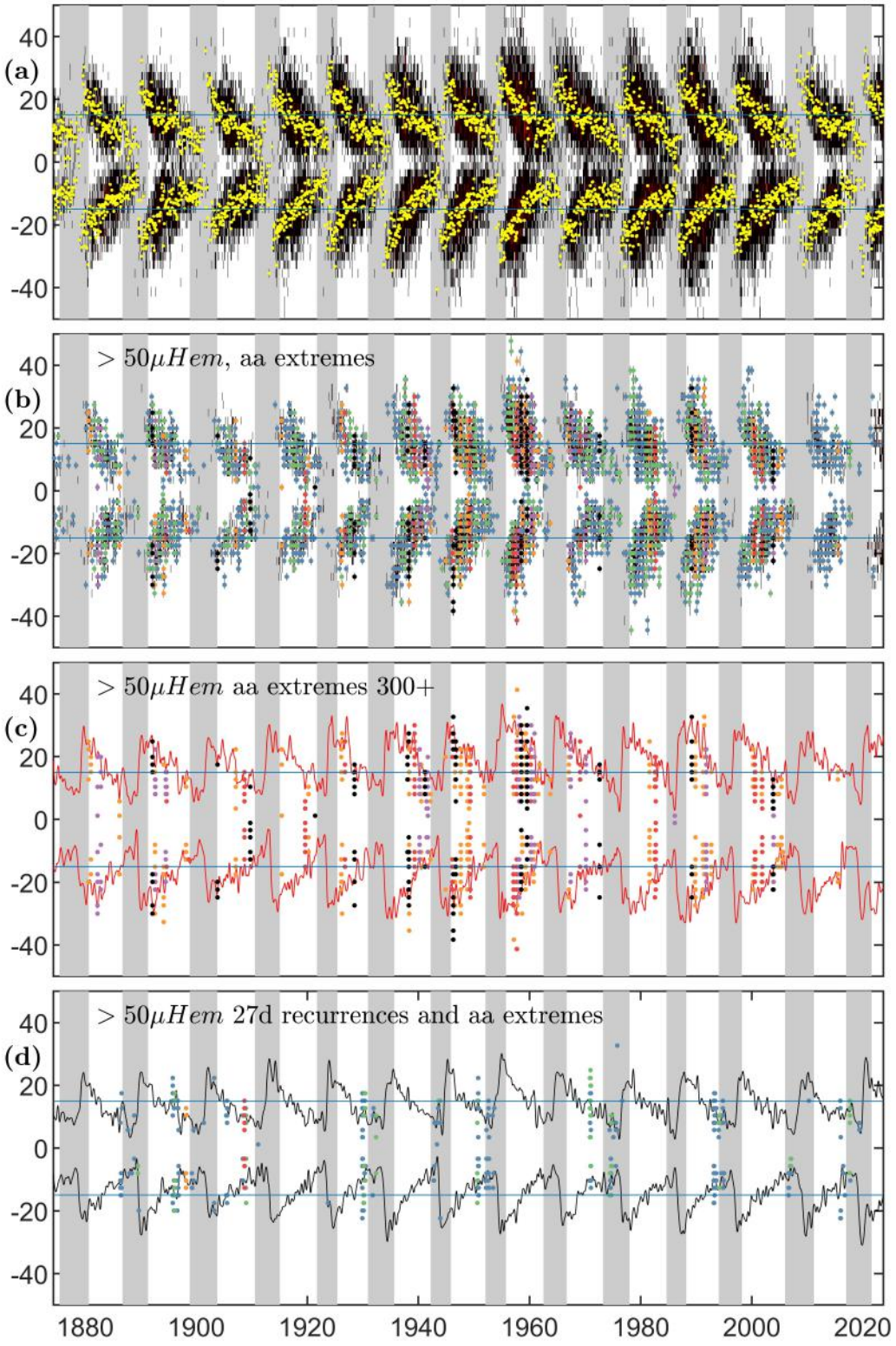

Extended Data 4 Sunspot area latitudes and extreme and recurrent geomagnetic activity overplotted for the last 13 solar cycles. All panels: latitude plotted as a function of time. Blue horizontal lines plot latitude ±15°. The quiet interval between the switch-off and in indicated by grey shading. Panel (a) total sunspot area in single Carrington rotation-latitude bins (black) overplotted with the area centroid for each Carrington rotation (yellow). Panel (b) overplots on all sunspot area latitude bins with area $> 50\mu Hem$ at the Carrington rotation during which the *aa* index exceeds a threshold of 100 (blue) 200 (green) 300 (orange) 400 (red) 500 (purple) 600 (black) nT. Panel (c) plots at all latitude bin centroids at the Carrington rotation during which the *aa* index exceeds a threshold of 300 (orange) 400 (red) 500 (purple) 600 (black) nT. The red lines plot 13 Carrington rotation smoothed latitudes below which 90% of total sunspot AR area lie. Panel (d) as for panel (b) for Carrington rotations where the *aa* index both exceeds the threshold and has a 27 day lag autocovariance exceeding 0.25. The black lines plot 20 Carrington rotation smoothed sunspot areas latitude centroids.